

Simultaneous dependence of the dark matter and gas clustering on the scale and environment

YUN WANG ¹, HUA-YU YANG ¹ AND PING HE ^{1,2}

¹College of Physics, Jilin University, Changchun 130012, P.R. China.

²Center for High Energy Physics, Peking University, Beijing 100871, P.R. China.

ABSTRACT

In this work, we propose new statistical tools that are capable of characterizing the simultaneous dependence of the matter clustering on the scale and density environment, which are the environment-dependent wavelet power spectrum (env-WPS) and environment-dependent wavelet cross-correlation (env-WCC). We apply these statistics to the projected 2D dark matter and baryonic gas density fields of the IllustrisTNG simulation at redshifts from $z = 3.0$ to $z = 0.0$. Measurement of the env-WPSs indicates that the clustering strengths of both the dark matter and gas increase with density. At all redshifts, we observe that the env-WPS of the gas is suppressed on intermediate and small scales, which is caused by baryonic processes. Furthermore, by computing the environmental bias function, we find that this suppression varies with the environment, scale and redshift. A noteworthy feature is that at $z = 0.0$, the bias value increases with density on scales $2 \lesssim k \lesssim 10 h\text{Mpc}^{-1}$, which is the reversal of that in earlier times. On the other hand, the env-WCC also shows strong environmental dependence on scales $k \gtrsim 2 h\text{Mpc}^{-1}$ and is sensitive to the redshift. We find that at $z = 3.0$, the coherence of the dark matter and gas decreases with density. At lower redshifts, the coherence in denser environments becomes much higher than that in less dense environments. These results suggest that baryonic processes have less effect on the matter clustering in high-density environments at later times. Obviously, these statistics provide us rich information and hence could improve our understanding of the matter clustering.

Unified Astronomy Thesaurus concepts: Wavelet analysis (1918); Dark matter (353); Intergalactic medium (813); Large-scale structure of the universe (902)

1. INTRODUCTION

In the standard paradigm of galaxy formation, small density fluctuations of baryonic gas start to grow and develop together with that of dark matter under the gravitational instability after recombination. At later times, dark matter fluctuations, once exceeding some threshold, will collapse into virialized halos, within which partial gas condenses and cools to form galaxies (Mo et al. 2010). Therefore galaxies are biased discrete tracers of the underlying matter distribution, while the gas, as a continuous fluctuating medium, may better trace the matter distribution. On the simulation side, many studies confirm that the baryonic gas follows the underlying dark matter distribution on large scales quite well. For example, the power spectrum of the gas density field is very close to that of dark matter (e.g. Cui & Zhang 2017; Springel et al. 2018), the spatial distributions of the dark matter and bary-

onic gas are highly correlated with each other over a wide range of scales (e.g. Yang et al. 2020, 2021), and the gas alone can be used to classify the cosmic web un-biased (e.g. Cui et al. 2018). Additionally, the intergalactic gas distribution is receiving increasing attention in observations. Measuring the large-scale structure of the Universe traced by the gas is the goal of the upcoming surveys, such as CHIME (Bandura et al. 2014), HIRAX (Newburgh et al. 2016) and SKA (Bacon et al. 2020).

As the scale becomes smaller, galaxy formation physics, such as gas cooling, star formation and feedback processes, have an increasing influence on the matter clustering, thereby resulting in a significant bias between the gas and dark matter. In particular, the clustering of gas is strongly suppressed up to scales a few times $0.1 h\text{Mpc}^{-1}$ mainly due to the active galactic nuclei (AGN) feedback, which heats and ejects gas from halos, while gas cooling and star formation could weaken this suppression on small scales (van Daalen et al. 2019). Moreover, it is well known that there is a strong relationship between galaxy's properties and its density environments. For instance, massive and quenched galaxies tend

to live in high-density environments (e.g. Hoyle et al. 2012; Moorman et al. 2016), and the star formation rates of galaxies increase with environmental density at redshifts $z \gtrsim 1$, but decrease with environmental density at redshifts $z \lesssim 1$ (e.g. Cooper et al. 2008; Wang et al. 2018; Hwang et al. 2019). The environmental dependence of galactic properties may imply two aspects. First, galaxies in high-density environments interact more frequently and therefore strip their gas faster than those in low-density environments. Second, feedback (e.g. AGN feedback) efficiency varies in different density environments. For example, Miraghaei (2020) found that in SDSS DR7 underdense regions have a higher fraction of thermal-mode AGN than overdense regions for the massive red galaxies, whereas kinetic-mode AGN prefers to reside in denser regions.

According to the above statements, the bias between the spatial clustering of the gas and that of the dark matter is expected to depend on both the scale and density environment. Quantifying such simultaneous dependence on the scale and environment would hopefully deepen our understanding of the extent to which baryonic gas follows the dark matter. To achieve this goal, statistical tools that can give the frequency information while retaining the spatial information are required. Theoretically, this job can be done using the windowed Fourier transform (WFT), discrete wavelet transform (DWT) or continuous wavelet transform (CWT). However, the fixed window width of the WFT results that it cannot provide appropriate resolution in both space and frequency, and for the DWT, its dyadic sampling of scales causes it to lack the translational invariance (Addison 2017). Compared to these two transforms, the CWT, which uses adaptive window and satisfies the translational invariance, obviously is more suitable for analyzing signals with complex structures, e.g. cosmic density fields.

The most criticized aspect of the CWT is that its computation consumes more time and resources than that of the DWT. However, the Fourier convolution theorem allows us to compute the CWT fastly by utilizing the fast Fourier transform (FFT) as an intermediate step (Torrence & Compo 1998). In addition to this, there are also many researches dedicated to the fast implementation of the CWT in real domain (Rioul 1991; Unser et al. 1994; Berkner & Wells 1997; Vrhel et al. 1997; Muñoz et al. 2002; Omachi & Omachi 2007; Patil & Abel 2009; Arizumi & Aksenova 2019). For example, Muñoz et al. (2002) decompose the wavelet function and signal as B-spline bases, therefore the CWT is converted into a convolution of two B-splines, which can be expressed analytically and has a lower number of operations. Omachi & Omachi (2007) achieve the fast computation of the CWT by representing the wavelet as a polynomial within its compact support interval. The most current algorithm proposed by

Arizumi & Aksenova (2019), which is used in this work, approximates the mother wavelet as piecewise polynomials.

In our previous work (Wang & He 2021), we developed a new method to design continuous wavelet, through which those wavelets are constructed by taking the first derivative of smoothing functions, e.g. the Gaussian function, with respect to the positive defined scale parameter. The convenience brought by this method is that the original signal can be reconstructed through a single integral of the continuous wavelet coefficients. Furthermore, Wang et al. (2021) introduced wavelet-based statistical quantities including the wavelet power spectrum, wavelet cross-correlation and wavelet bicoherence, to characterize the clustering of the one dimensional matter distribution. The results of Wang et al. (2021) suggest that those wavelet statistics can correctly identify the clustering properties between different local regions at multiple scales, which means that we can further generalize them to examine the environmental effects at different scales for cosmological data in higher dimension.

Motivated by the findings of Wang et al. (2021), this paper will explore whether there is any environmental dependence of the clustering bias between the dark matter and baryonic gas at various scales. To this end, we construct two environment-dependent statistics built from the continuous wavelet coefficients, which are the environment-dependent wavelet power spectrum (env-WPS) and wavelet cross-correlation function (env-WCC), respectively. The env-WPS measures the matter clustering strength across different scales within a density bin, and the env-WCC measures the statistical coherence between spatial distributions of two matter components. For achieving a better performance in spectral analysis, the analytic wavelet function we used here is derived from the Gaussian function weighted by a cosine function, which has a better frequency resolution than the Gaussian-derived wavelet used in previous works (Wang & He 2021; Wang et al. 2021). In this preliminary study, we apply the env-WPS and env-WCC to the projected two-dimensional (2D) density fields of the IllustrisTNG100-1 simulation (Nelson et al. 2019).

The rest of this work is structured as follows. We describe the IllustrisTNG simulation suite briefly, and introduce the fundamental theories in Section 2. Our main results regarding the dependence of the matter clustering on both the scale and environment are given and discussed in Section 3. Finally in Section 4, we summarize our work and present the conclusions.

2. DATA AND METHODS

2.1. *IllustrisTNG*

The IllustrisTNG (hereafter TNG) is one of the state-of-the-art cosmological magneto-hydrodynamical simulations (Marinacci et al. 2018; Naiman et al. 2018; Nelson et al.

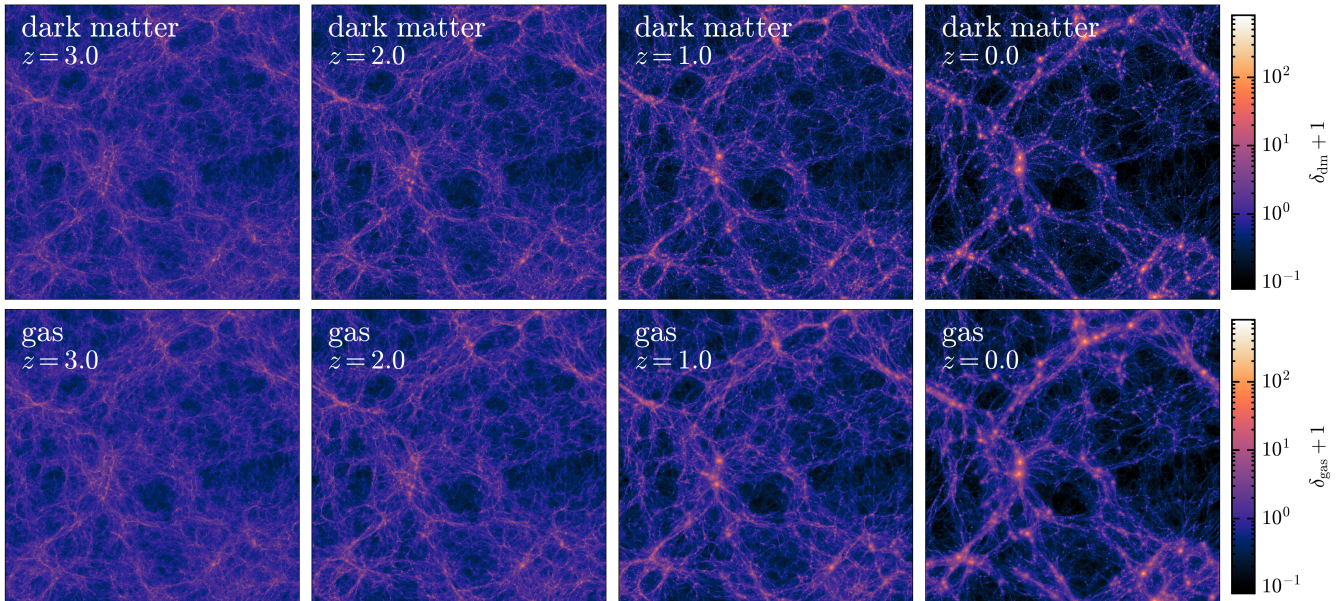


Figure 1. 2D density fields of dark matter and baryonic gas in TNG100-1, at redshifts $z = 3, 2, 1$ and 0 arranged from left to right. In each panel, density field is in a slice of width $75 h^{-1}\text{Mpc}$ and thickness $16 h^{-1}\text{Mpc}$, and is normalized to the respective mean density. By visual inspection, we see that the density field of the gas is smoother than that of the dark matter at $z = 0$, while they are much more similar to each other at higher redshifts.

Table 1. Abbreviations used in the paper, with their meanings

| Abbreviation | Meaning |
|--------------|-------------------------------------------------|
| CWT | continuous wavelet transform |
| GDW | Gaussian-derived wavelet |
| CW-GDW | cosine weighted Gaussian-derived wavelet |
| WPS | wavelet power spectrum |
| WCC | wavelet cross-correlation |
| env-WPS | environment-dependent wavelet power spectrum |
| env-WCC | environment-dependent wavelet cross-correlation |

2018, 2019; Pillepich et al. 2018a; Springel et al. 2018), which is executed with the AREPO code (Springel 2010) and consists of three simulation volumes: TNG300, TNG100, TNG50. All these runs assume Planck-concordance cosmology (Planck Collaboration XIII 2016), i.e. $\Omega_\Lambda = 0.6911$, $\Omega_m = \Omega_{\text{dm}} + \Omega_b = 0.3089$, $\Omega_b = 0.0486$, $\sigma_8 = 0.8159$, $n_s = 0.9667$, $h = 0.6774$. Compared with earlier Illustris simulations (Nelson et al. 2015; Vogelsberger et al. 2014), TNG, which uses updated physical models and numerical methods, yields better consistency with available observations of galaxy formation and evolution. Thus it provides us with an ideal laboratory to test theoretical models and de-

velop new analysis tools to achieve a more precise understanding of the structure formation and galaxy formation. The details about the IllustrisTNG model for galaxy formation are given in Pillepich et al. (2018b) and Weinberger et al. (2018).

In this work, we only use the snapshots of TNG100-1 simulation at redshifts $z = 0.0, 1.0, 2.0$ and 3.0 . This simulation adopts a periodic box of side length $L_{\text{box}} = 75 h^{-1}\text{Mpc} \simeq 110 \text{ Mpc}$, and contains 1820^3 dark matter particles of mass $\sim 7.5 \times 10^6 M_\odot$ and the same number of initial gas cells with average mass $\sim 1.4 \times 10^6 M_\odot$. Therefore, TNG100-1 reaches the best compromise between a large volume and resolution. Since we restrict ourselves to analyze 2D matter distribution, we first interpolate mass points to 1024^3 regular grids using the cloud-in-cell assignment scheme. Then we obtain the 2D density fields by averaging the 3D density fields along z -axis over $16 h^{-1}\text{Mpc}$. The resulting projected density fields for the dark matter and baryonic gas are shown in Fig. 1.

2.2. Cosine weighted Gaussian-derived wavelet and Continuous wavelet analysis

In previous works (Wang & He 2021; Wang et al. 2021), we applied the Gaussian-derived wavelet (a low-oscillation wavelet, abbreviated as GDW) to the spectral analysis of the matter clustering in one dimensional case. However, low-oscillation wavelets are more extended in Fourier space, which can make the results of spectral analysis at small scales contaminated by large scales (Frick et al. 2001). For achiev-

ing a better separation of scales, we take the Gaussian function weighted by a cosine as the smoothing function and then derive the wavelet from it. In one dimension, the form of such cosine weighted Gaussian-derived wavelet (CW-GDW) is shown below,

$$\begin{aligned}\psi(w, x) &\equiv \sqrt{w} \frac{\partial g_{\cos}(w, x)}{\partial w} \\ &= \sqrt{\frac{w}{2\pi\alpha^2}} \left[\left(1 - \left(\frac{wx}{\alpha} \right)^2 \right) \cos\left(\frac{wx}{\alpha}\right) \right. \\ &\quad \left. - \left(\frac{wx}{\alpha} \right) \sin\left(\frac{wx}{\alpha}\right) \right] \exp\left(-\frac{1 - \left(\frac{wx}{\alpha}\right)^2}{2}\right),\end{aligned}\quad (1)$$

and its Fourier transform is

$$\begin{aligned}\hat{\psi}(w, k) &= \frac{1}{\sqrt{w}} \left(\frac{\alpha k}{w} \right) \left[\left(\frac{\alpha k}{w} \right) \cosh\left(\frac{\alpha k}{w}\right) \right. \\ &\quad \left. - \sinh\left(\frac{\alpha k}{w}\right) \right] \exp\left(-\frac{1}{2} \left(\frac{\alpha k}{w} \right)^2\right),\end{aligned}\quad (2)$$

where the dimensionless constant α is approximately equal to 2.20473 used to set w to be the peak frequency of $\hat{\psi}(w, k)$, and $g_{\cos}(w, x) = w \exp\left(-\frac{1 - (wx/\alpha)^2}{2}\right) \times \cos(wx/\alpha) / \sqrt{2\pi\alpha^2}$ is the cosine weighted Gaussian smoothing function. Compared to the GDW, the CW-GDW has a better spectral resolution as shown in Fig. 2.

Following the logic of Wang & He (2021), the 2D CW-GDW can be obtained as

$$\begin{aligned}\Psi(\mathbf{w}, \mathbf{r}) &= \sqrt{w_x w_y} \frac{\partial^2 G_{\cos}(\mathbf{w}, \mathbf{r})}{\partial w_x \partial w_y} \\ &= \sqrt{w_x} \frac{\partial g_{\cos}(w_x, x)}{\partial w_x} \sqrt{w_y} \frac{\partial g_{\cos}(w_y, y)}{\partial w_y} \\ &= \psi(w_x, x) \psi(w_y, y),\end{aligned}\quad (3)$$

where $G_{\cos}(\mathbf{w}, \mathbf{r}) = g_{\cos}(w_x, x) g_{\cos}(w_y, y)$ is the 2D cosine weighted Gaussian smoothing function with $\mathbf{r} = (x, y)$, and $\mathbf{w} = (w_x, w_y)$ is the scale vector. As illustrated in Fig. 3, the 2D CW-GDW is an anisotropic wavelet. Then the 2D CWT is defined as the convolution between a field $f(\mathbf{r})$ and the analytic wavelet $\Psi(\mathbf{w}, \mathbf{r})$, which is given by

$$W_f(\mathbf{w}, \mathbf{r}) = \int_{\mathbb{R}^2} f(\mathbf{r}') \Psi(\mathbf{w}, \mathbf{r} - \mathbf{r}') d^2 \mathbf{r}',\quad (4)$$

in which the symbol \mathbb{R}^2 represents the 2D real vector space. $f(\mathbf{r})$ can be reconstructed by the formula below

$$f(\mathbf{r}) = \int_{\mathbb{R}_+^2} \frac{W_f(\mathbf{w}, \mathbf{r})}{\sqrt{w_x w_y}} d^2 \mathbf{w},\quad (5)$$

which is the extension of the 1D reconstruction formula given in Wang et al. (2021), and \mathbb{R}_+^2 represents the 2D positive real vector space.

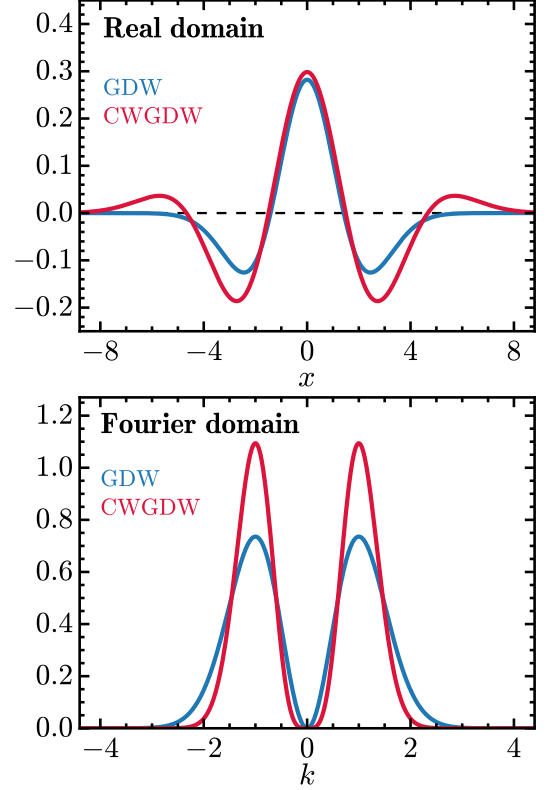


Figure 2. Comparison of the one-dimensional GDW and CW-GDW on real (top) and Fourier domain (bottom) at scale $w = 1$. For presentation convenience, all variables are dimensionless.

2.3. The env-WPS and env-WCC of the cosmic density fields

At each redshift, we compute the CWTs of density fields via the fast algorithm in real domain proposed recently by Arizumi & Aksenova (2019), we refer the readers to it for details. To measure the clustering strength of the dark matter and gas in different environments, their env-WPSs are computed from wavelet coefficients as below

$$P_{\text{dm}}^W(w, \delta) = \left\langle |W_{\text{dm}}(\mathbf{w}, \mathbf{r})|^2 \right\rangle_{\Delta w, \Delta \delta} \quad (6)$$

and

$$P_{\text{gas}}^W(w, \delta) = \left\langle |W_{\text{gas}}(\mathbf{w}, \mathbf{r})|^2 \right\rangle_{\Delta w, \Delta \delta}, \quad (7)$$

where $W_{\text{dm}}(\mathbf{w}, \mathbf{r})$ and $W_{\text{gas}}(\mathbf{w}, \mathbf{r})$ are the CWTs of the dark matter and gas density fields respectively, ' $\langle \dots \rangle_{\Delta w, \Delta \delta}$ ' denotes the statistical averaging among all \mathbf{w} and $\delta(\mathbf{r})$ contained in the bins $[w - \Delta_w/2, w + \Delta_w/2]$ and $[\delta - \Delta_\delta/2, \delta + \Delta_\delta/2]$, and $\delta(\mathbf{r}) = (\Omega_{\text{dm}} \delta_{\text{dm}}(\mathbf{r}) + \Omega_{\text{b}} \delta_{\text{gas}}(\mathbf{r})) / \Omega_{\text{m}}$ is the total matter overdensity¹.

¹ We simply use the gas overdensity here to refer to the total baryon overdensity, since most of the baryons are in gaseous form (Bregman 2007).

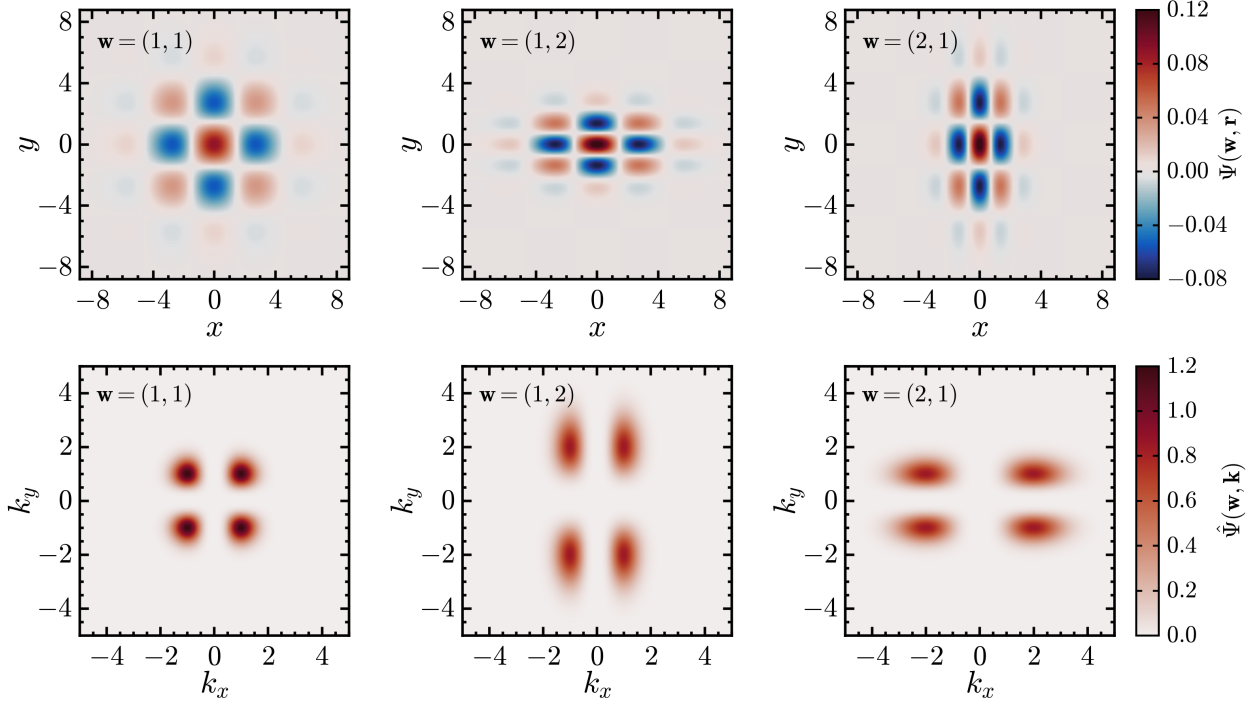


Figure 3. Two dimensional CW-GDW $\Psi(\mathbf{w}, \mathbf{r})$ (top panels) and its Fourier transform (bottom panels) at three scales $\mathbf{w} = (1, 1)$, $(1, 2)$ and $(2, 1)$. For presentation convenience, all variables are dimensionless.

The env-WCC between the dark matter and gas distributions is defined as

$$C_{\text{dm,gas}}^W(w, \delta) = \frac{P_{\text{dm,gas}}^W(w, \delta)}{\sqrt{P_{\text{dm}}^W(w, \delta)P_{\text{gas}}^W(w, \delta)}}, \quad (8)$$

where $P_{\text{dm,gas}}^W(w, \delta) = \langle W_{\text{dm}}(\mathbf{w}, \mathbf{r})W_{\text{gas}}(\mathbf{w}, \mathbf{r}) \rangle_{\Delta w, \Delta \delta}$. It is a measure of statistical coherence between these two fields, and takes on values between 1 and -1 . If $C_{\text{dm,gas}}^W(w, \delta) = 1$, then the fields are totally correlated. On the other hand, if $C_{\text{dm,gas}}^W(w, \delta) = -1$, then the fields are totally anti-correlated.

If we expand the overdensity bin to include all overdensities, then the global WPSs and WCC are

$$P_{\text{dm}}^W(w) = \langle |W_{\text{dm}}(\mathbf{w}, \mathbf{r})|^2 \rangle_{\Delta w, \text{all } \delta(\mathbf{r})} \quad (9)$$

$$P_{\text{gas}}^W(w) = \langle |W_{\text{gas}}(\mathbf{w}, \mathbf{r})|^2 \rangle_{\Delta w, \text{all } \delta(\mathbf{r})} \quad (10)$$

and

$$C_{\text{dm,gas}}^W(w) = \frac{P_{\text{dm,gas}}^W(w)}{\sqrt{P_{\text{dm}}^W(w)P_{\text{gas}}^W(w)}}, \quad (11)$$

in which

$$P_{\text{dm,gas}}^W(w) = \langle W_{\text{dm}}(\mathbf{w}, \mathbf{r})W_{\text{gas}}(\mathbf{w}, \mathbf{r}) \rangle_{\Delta w, \text{all } \delta(\mathbf{r})}.$$

Finally, We need to determine the correspondence between the wavelet scale and Fourier wavenumber in the CW-GDW case. According to the method given in Section 2.5 of Wang et al. (2021), the relationship between the scale number w and the equivalent Fourier wavenumber k is

$$w \approx 0.94411k. \quad (12)$$

Hereafter, we will use k to denote the clustering scale.

3. RESULTS AND DISCUSSION

In this section, we present our main results and discussions on the dark matter and baryonic gas clustering at redshifts $0 \leq z \leq 3$. In particular, we compare the Fourier power spectrum with the global wavelet power spectra based on the GDW and CW-GDW. Furthermore, we explore how the dark matter and gas clustering strengths depend on the environment by computing the env-WPSs, and we also quantify the deviation between dark matter and gas distributions by computing the environmental bias and env-WCC.

3.1. The global wavelet analysis and conventional Fourier analysis

Until now, we have designed two kinds of wavelets, i.e. the GDW and CW-GDW. Before further analysis, we check whether these two wavelets could reproduce the Fourier power spectrum, and it is important to do so since most works on matter clustering is done by Fourier analysis. To

do this, we create a 2D Gaussian random field with a given power-law power spectrum $P(k) = 0.1k^{-2}$ and make a comparison between its measured Fourier and global wavelet power spectra. As shown in the bottom left panel of Fig. 4, both wavelet power spectra with GDW and CW-GDW, as well as Fourier power spectrum, converge to the power-law power spectrum. Then we measure the Fourier and global wavelet power spectra of the 2D density field of the dark matter at $z = 0$, results of which are shown in the bottom right panel of Fig. 4. It can be seen that all power spectra have the same shape and amplitude qualitatively. Therefore, the wavelet power spectrum can also correctly characterize the matter distribution. Nevertheless, the use of different analytic wavelet can lead to subtle differences in the results. Although this is not obvious for the random field, the GDW power spectrum is slightly lower than both the Fourier and CW-GDW power spectra on the scales $k \lesssim 3 h\text{Mpc}^{-1}$, and higher on $k \gtrsim 20 h\text{Mpc}^{-1}$ for the highly non-linear dark matter density field. This is due to the poor localization of the GDW in frequency domain, which is discussed in Section 2.2. Overall, the global wavelet power spectrum based on the CW-GDW is closer to the Fourier power spectrum than that based on the GDW, especially on small scales. In the following, we will explore the environmental effects on the matter clustering using the CW-GDW.

3.2. The environment-dependent bias of the gas relative to the dark matter

We first focus the env-WPSs of the dark matter and baryonic gas density fields at redshifts $z = 3, 2, 1$ and 0, as shown in the Fig.5. Now let us consider the behavior of the dark matter. At redshift $z = 3$, WPSs in different environments already exhibit different clustering strengths, except that on the largest scales where they all converge to the global WPS. Specifically, the env-WPS is monotonically increasing towards higher density environments on almost all scales and the global one lies between those of overdense and underdense environments. This result is intuitive because high-density environments contain more gravitationally bound objects (e.g. halos and subhalos) than low-density environments (Maulbetsch et al. 2007). At lower redshifts, the env-WPS continues to maintain the same dependence on the density environment with enhanced amplitude mainly due to non-linear gravitational effects. For the gas component, its env-WPS exhibits similar features to that of the dark matter. However, on intermediate and small scales, the env-WPS of the gas are suppressed, which is caused by baryonic processes resisting the collapse of gas, particularly active galactic nuclei (AGN) feedback (van Daalen et al. 2019).

To further quantify differences between the baryonic gas and dark matter clustering at various scales and environments, we define the environmental bias function as the

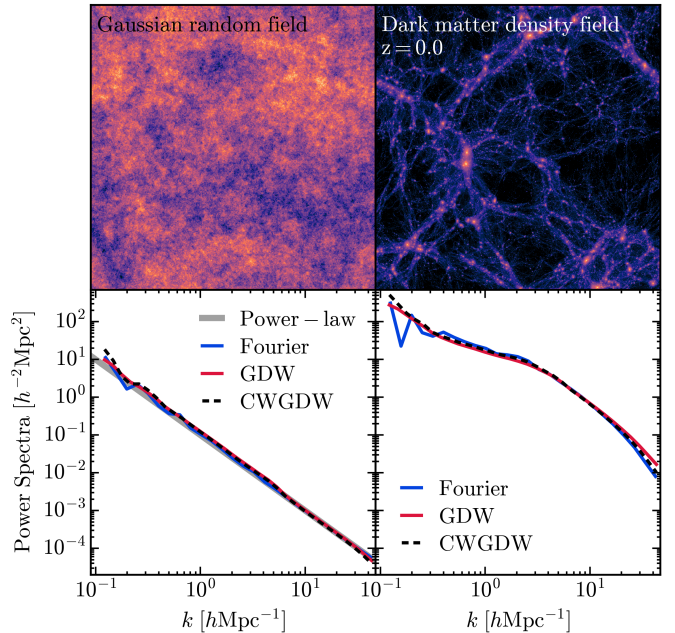


Figure 4. Comparison of Fourier power spectra and global wavelet power spectra. Top left: 2D Gaussian random field with power-law power spectrum $P(k) = 0.1k^{-2}$. Bottom left: the measured power spectra of the random field. Top right: the slice of the dark matter density field at redshift $z = 0$. Bottom right: the measured power spectra of the dark matter density field. In these two bottom panels, all wavelet power spectra are multiplied by some constant to fit the Fourier power spectrum.

square root of the ratio between the env-WPSs of the gas and dark matter,

$$b^W(k, \delta) \equiv \sqrt{\frac{P_{\text{gas}}^W(k, \delta)}{P_{\text{dm}}^W(k, \delta)}}, \quad (13)$$

which is scale-dependent and environment-dependent. For comparison, we use $b^W(k) = \sqrt{P_{\text{gas}}^W(k)/P_{\text{dm}}^W(k)}$ to represent the global bias of the baryonic gas relative to the dark matter.

In Fig. 6, we show the environmental bias $b^W(k, \delta)$ versus scale at given densities, and $b^W(k, \delta)$ versus density at given scales are presented in Fig. 7. we see from these two figures that the environmental bias function $b^W(k, \delta)$ is almost independent of the density environment and converges to the global bias on very large scales at all epochs. As the scale gets smaller, the environment dependence of the bias becomes increasingly prominent with decreasing scale. More detailedly, we see that at redshifts $z = 3$, the environmental bias decreases monotonically as the density increases on scales $0.3 \lesssim k \lesssim 10 h\text{Mpc}^{-1}$, which may reflect that the feedback processes are more effective in denser environments at this epoch and hence the clustering of the gas is more suppressed in such environments. We observe that the

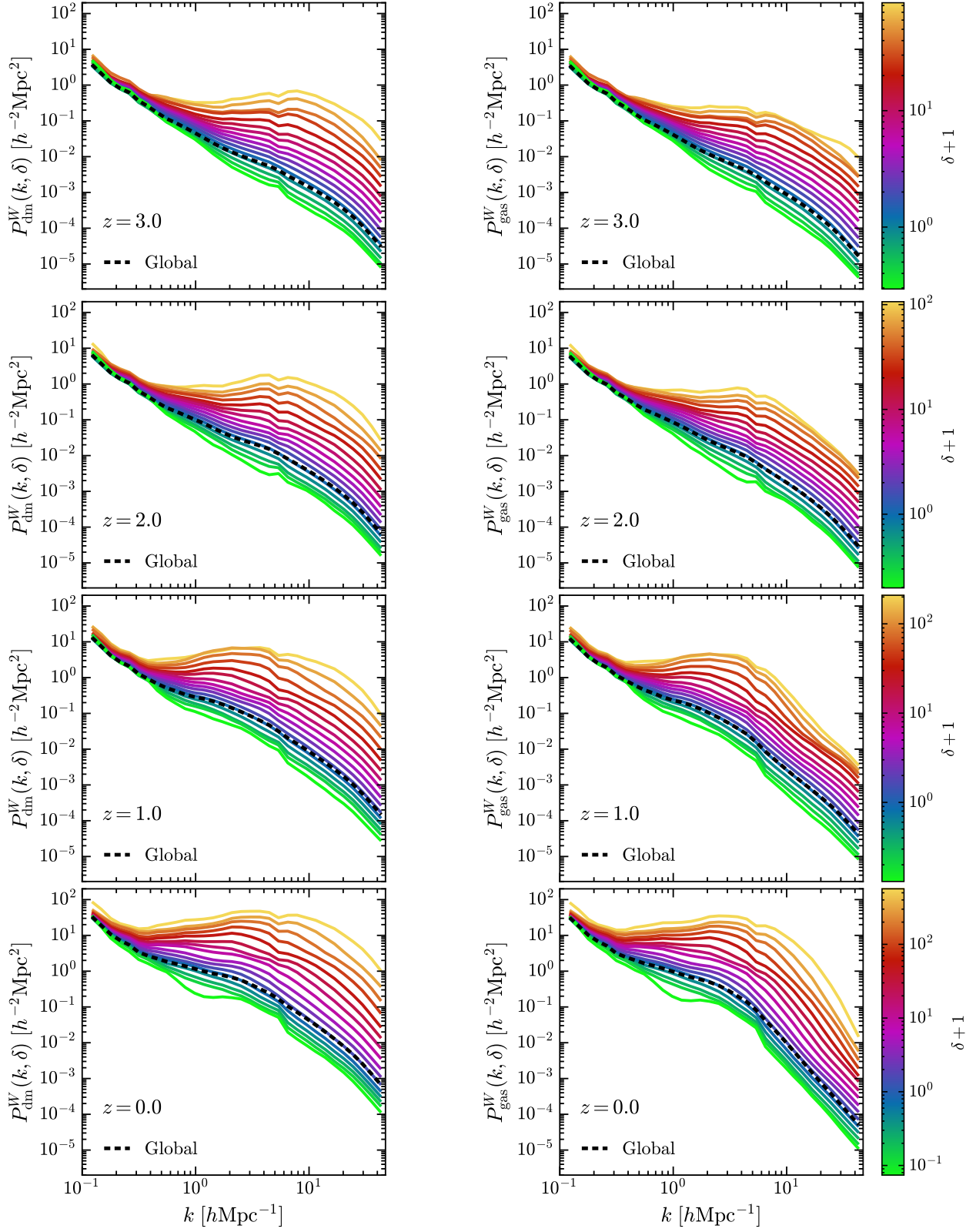


Figure 5. Redshift evolution of the env-WPSs for the dark matter distribution (left column) and baryonic gas distribution (middle column) from $z = 3$ to $z = 0$. The color of each solid line indicates the value of the overdensity. In each panel, the global WPS is plotted as a dashed black line for comparison.

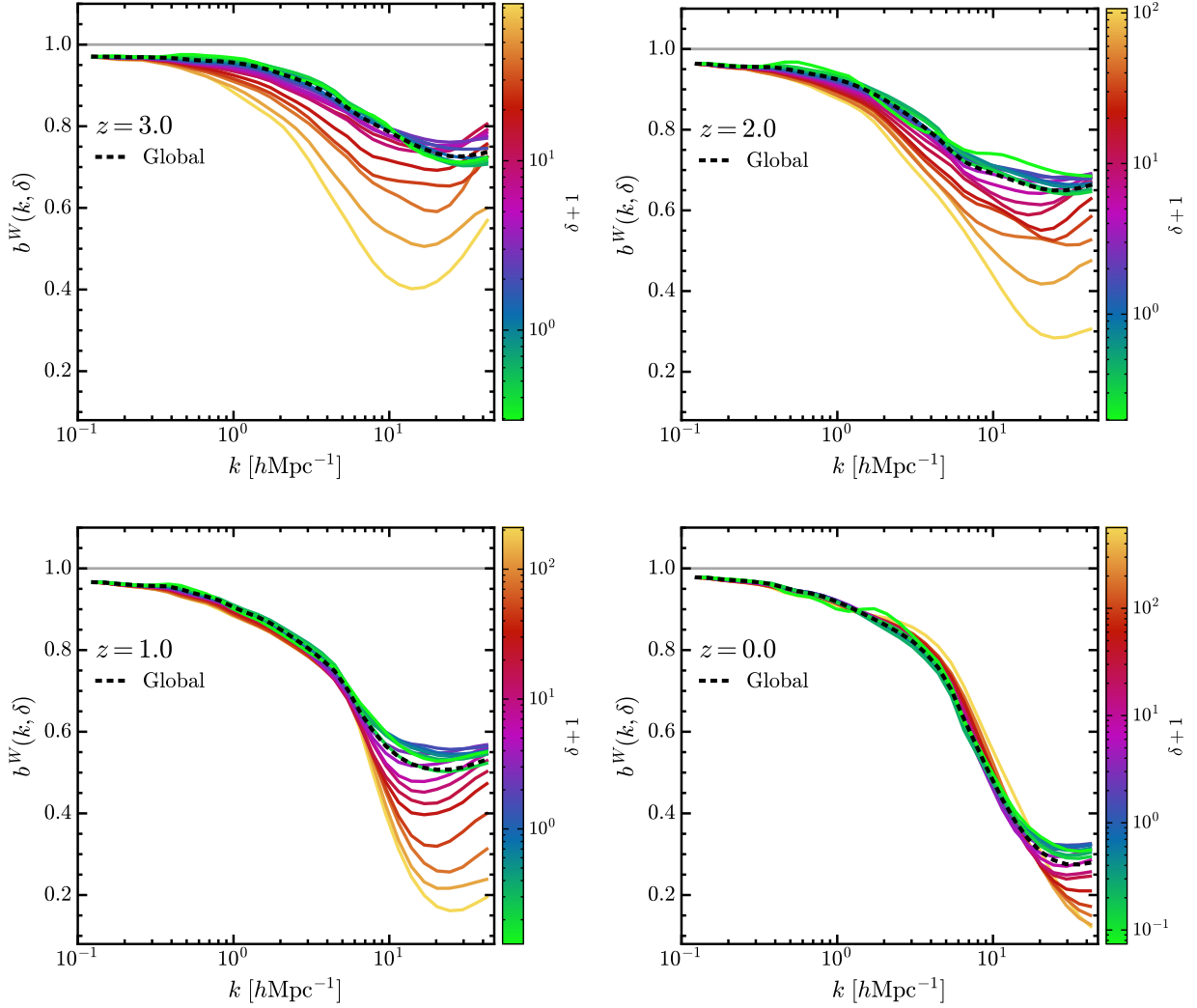


Figure 6. Environment-dependent bias of the distribution of the gas relative to that of dark matter, computed by equation (13). In this figure, the environmental bias $b^W(k, \delta)$ is displayed as a function of scale k for different density environments at redshifts $z = 3, 2, 1$ and 0 . For reference, the dashed black line gives the global bias.

monotonically decreasing of the environmental bias with increasing density becomes weaker and weaker towards lower redshifts. At redshift $z = 1$, the environmental bias function hardly varies with the density on scales $k \lesssim 10$ hMpc $^{-1}$. By the time of $z = 0$, the environmental bias even shows a tendency to increase with increasing density from 2 hMpc $^{-1}$ to 10 hMpc $^{-1}$. This redshift evolution of the environmental bias on scales of $k \lesssim 10$ hMpc $^{-1}$ may reveal that the feedback strength in denser environments is reduced more severely than that in less dense environments at low redshifts, and the gas in denser environments can be preferentially re-accreted to halos.

The relationship between the bias $b^W(k, \delta)$, scale and density environment is more complex on $k \gtrsim 10$ hMpc $^{-1}$, where the effect of gas cooling and star formation starts to become dominant. On this scale range, it can be seen

that at redshifts $z \geq 1$, the curves for the environmental bias vs scale experience an apparent upturn in overdensities $\delta + 1 \gtrsim 3$, while those curves in lower density environments are much flatter. This result reflects that star-forming activities in denser environments are more intense than those in lower density environments. At present day ($z = 0$), the environmental bias vs scale shows no upturn in overdensities $\delta + 1 \gtrsim 20$, while tiny upturn is observed in lower densities. This reflect that in lower redshifts, the star formation rate is lower in denser environments. These results are roughly consistent with the findings of Hwang et al. (2019), which use the IllustrisTNG simulation to study the time evolution of star formation rate (SFR)–density relation. They find that the SFR of galaxies increases with local density at $z \geq 1$, whereas decreases with local density at $z = 0$. In addition, we see from Fig. 7 that on small

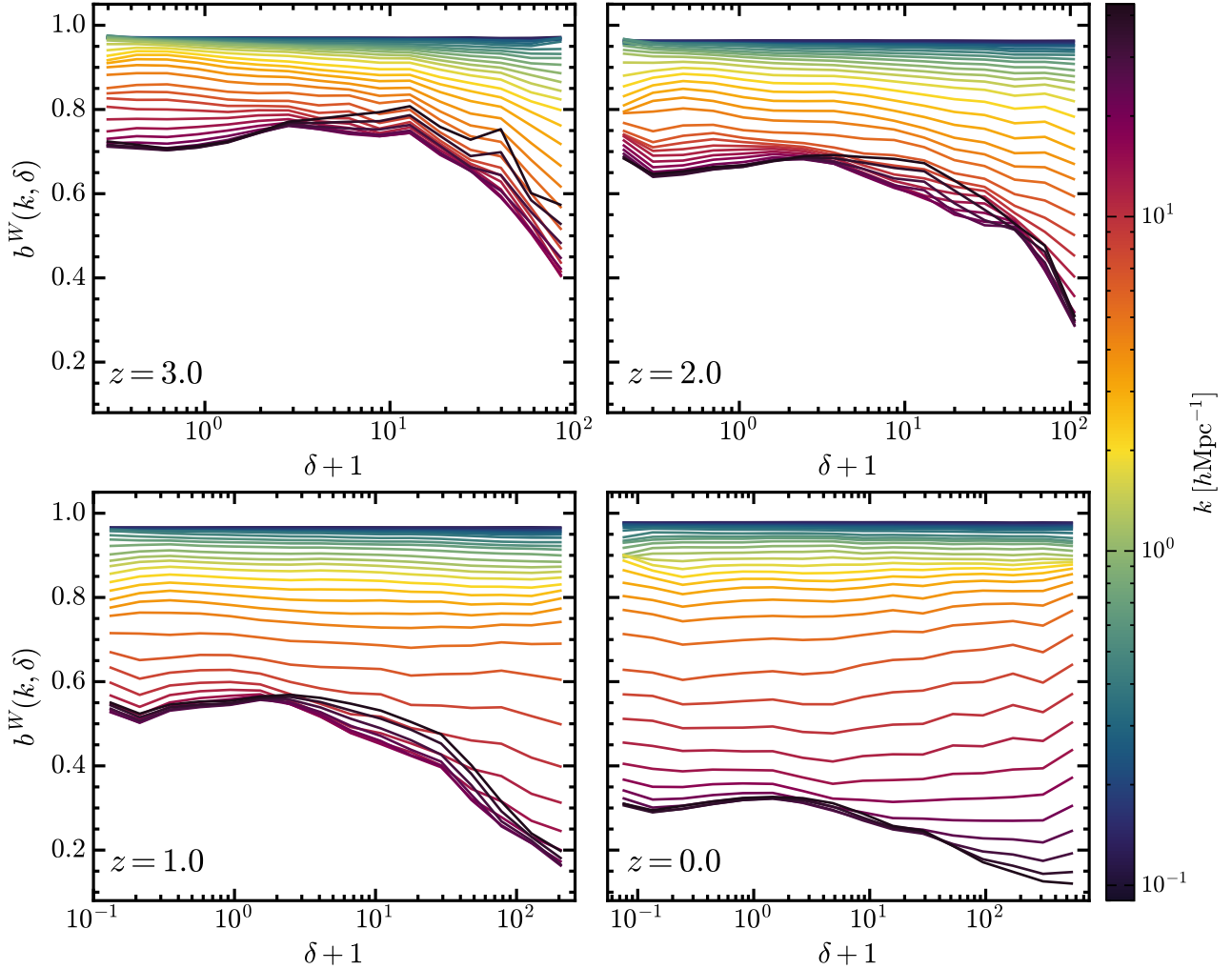


Figure 7. The environmental bias $b^W(k, \delta)$ versus overdensity δ at various scales indicated by the colorbar. This figure expresses the same thing as Fig. 6, but from a different perspective.

scales $k \gtrsim 10 \text{ hMpc}^{-1}$, $b^W(k, \delta)$ decreases significantly with density in high-density environments, while varies little with density in low-density environments. This result is consistent the fact that denser environments host higher fractions of quenched galaxies (e.g., see Hoyle et al. 2012; Moorman et al. 2016).

3.3. The env-WCC between the dark matter and gas distributions

The evolutions of the env-WCC versus scale and versus density with time are shown in Figs. 8 and 9, respectively. As a comparison, the global WCC is also given in Fig. 8. We see that both the global and environmental WCCs are very close to one on large scales ($k \lesssim 2 \text{ hMpc}^{-1}$) for all redshifts, which means that distributions of the gas and dark matter are highly coherent on large scales. On smaller scales ($k \gtrsim 2 \text{ hMpc}^{-1}$), the global WCC starts to be less than one and decreases as the scale decreases, which is due to the re-

distribution of the dark matter and gas caused by baryonic physical processes.

Moreover, the env-WCC shows a strong environmental dependence on small scales. At all redshifts we consider, the env-WCC in less dense environments ($\delta + 1 \lesssim 3$) is closer to the global WCC. In denser environments ($\delta + 1 \gtrsim 3$), the env-WCC deviates more from the global WCC. At redshift $z = 3$, the env-WCC roughly decreases with increasing density on scales of $k \gtrsim 2 \text{ hMpc}^{-1}$. However, at redshift $z = 2$, the env-WCC in denser environments ($\delta + 1 \gtrsim 10$) appears to increase with increasing density on the scale range of $2 \lesssim k \lesssim 10 \text{ hMpc}^{-1}$, and this increasing trend extends to smaller scales and lower densities at later times. From the above results, we infer that at the earlier epoch ($z = 3$), the deviation between spatial distributions of the gas and dark matter in denser environments is more pronounced than that in less dense environments, which may imply that at this epoch, baryonic physical processes play a more vital role

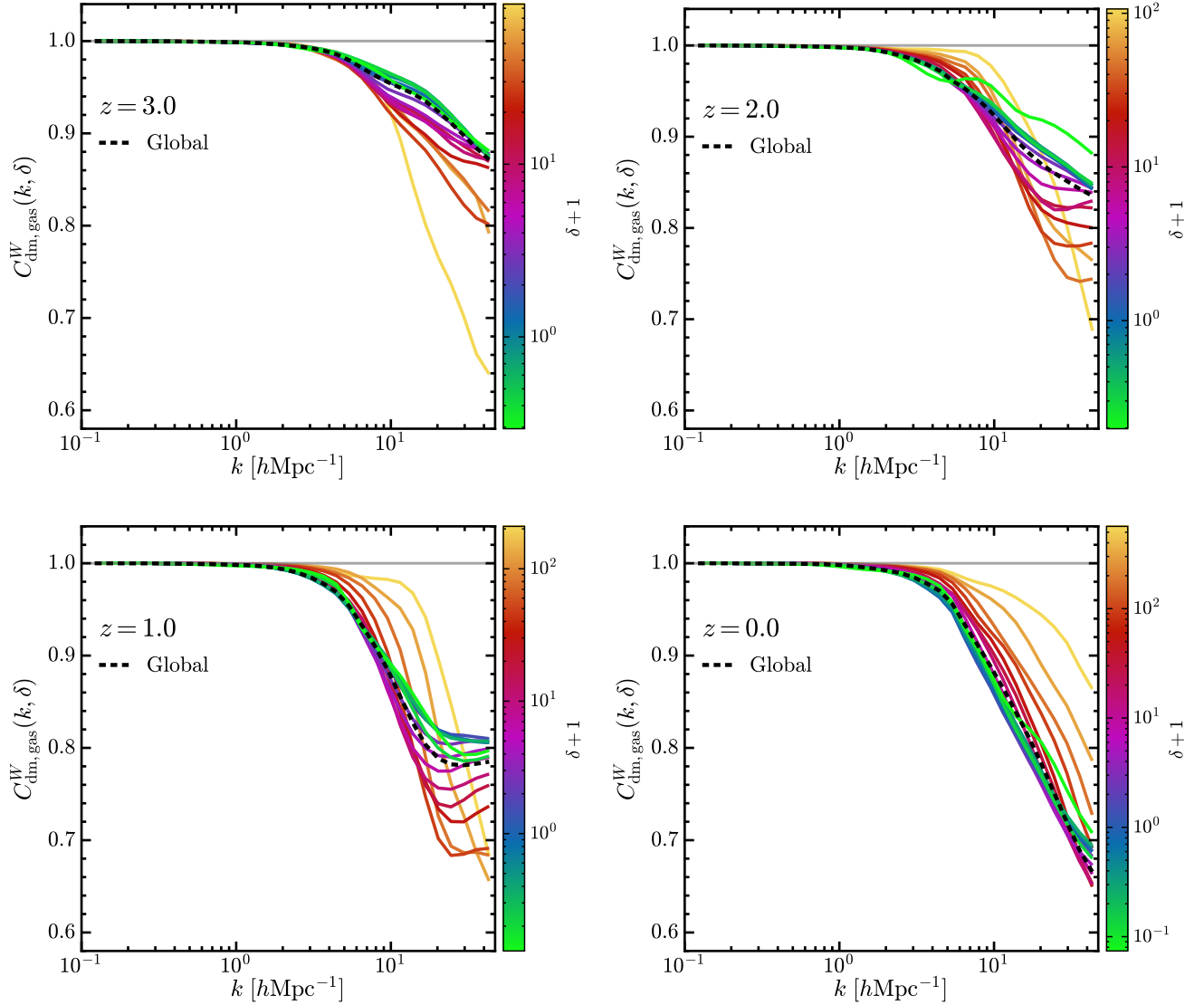


Figure 8. Redshift evolution of the env-WCC between the dark matter and gas density fields from $z = 3$ to $z = 0$. The color of each solid line indicates the value of the overdensity. In each panel, the global WCC is plotted as a dashed black line for comparison.

in denser environments than in less dense environments. As the redshift decreases, the gas in the dense environment follows the dark matter more and more closely than that in low-density environments, implying that the intensity of baryonic processes in high-density environments decreases with decreasing redshift, while that in low-density environments increases with decreasing redshift.

4. SUMMARY AND CONCLUSIONS

In this paper, we proposed two-dimensional wavelet based statistical tools: (1) the env-WPS, and (2) the env-WCC. These two statistics are built from the continuous wavelet coefficients, which retains the spatial and scale information simultaneously. Therefore we expect the env-WPS and env-WCC can quantify the density environment effects on the

matter clustering at various scales. To verify this, we apply the env-WPS and env-WCC to the 2D projected dark matter and gas density fields of the TNG100-1 simulation. To achieve a better spectral analysis, we use the cosine weighted Gaussian-derived wavelet, defined by equation (1), as our analytic wavelet. Compared to the Gaussian-derived wavelet used in our previous works, this new wavelet has a higher resolution in the frequency domain, and therefore the global wavelet power spectrum based on it is much more close to the Fourier power spectrum particularly on small scales, as shown in Fig. 4.

This study has confirmed that the env-WPS and env-WCC are able to correctly characterize the dependence of the matter clustering on both scale and environment. Firstly, we identify that the env-WPSs of the dark matter and gas show

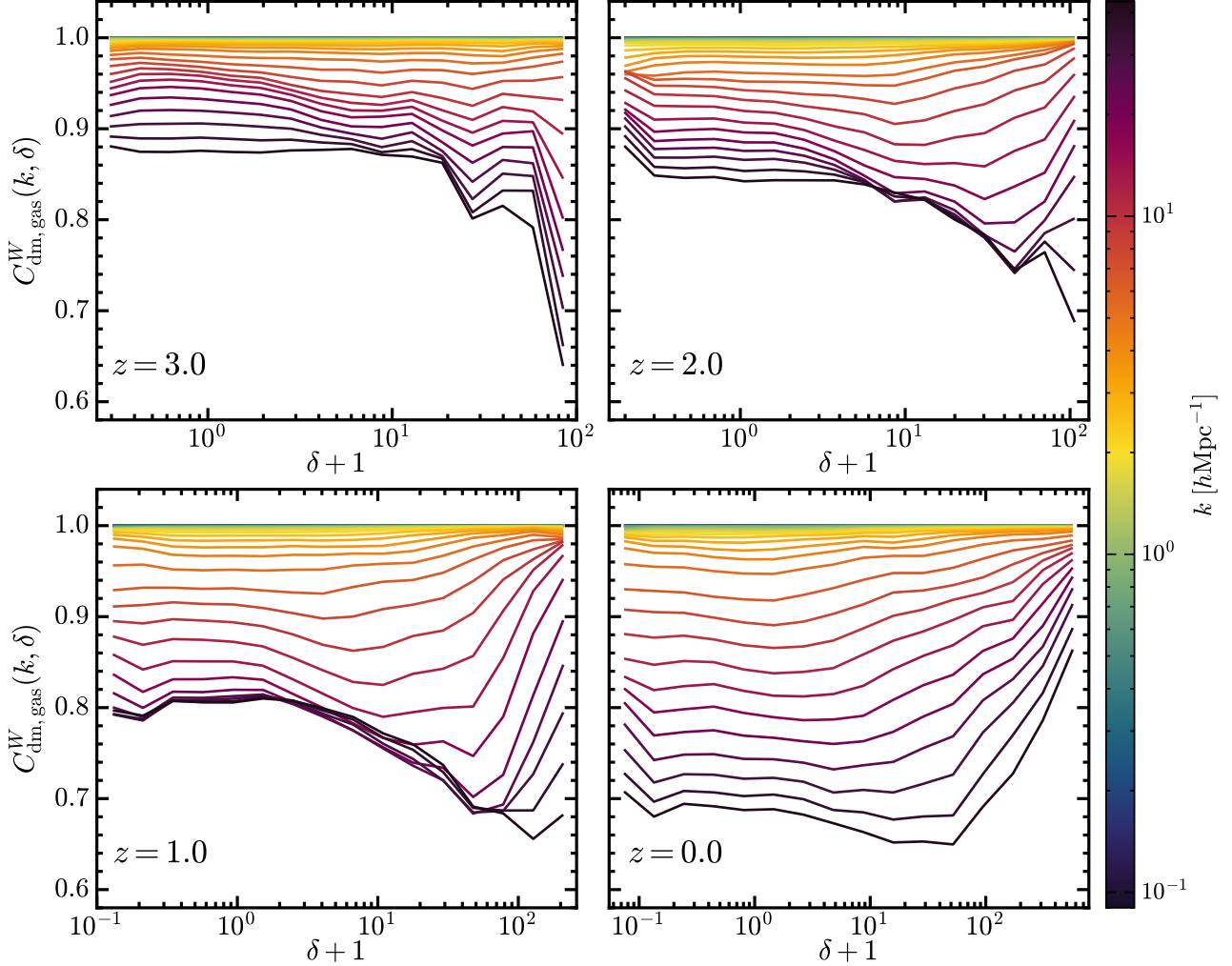


Figure 9. The env-WCC $C_{\text{dm,gas}}^W(k, \delta)$ versus overdensity δ at various scales indicated by the colorbar. This figure expresses the same thing as Fig. 8, but from a different perspective.

similar features: they both converge to the global WPS at large scales, while at small scales they increase with increasing density (see Fig. 5). This environmental dependence becomes stronger as the redshift decreases, which is caused by the non-linear gravitational evolution. We also see that the env-WPS of the gas is suppressed on intermediate and small scales compared to that of the dark matter, which is caused by the baryonic physical processes. The suppression of the gas clustering in different density environments can be further quantified by the environment-dependent bias function defined by equation (13). In Figs. 6 and 7, we notice that at redshifts $z = 3$, the environmental bias decreases with increasing density from scales of few times $0.1 h\text{Mpc}^{-1}$ to $10 h\text{Mpc}^{-1}$, indicating the gas clustering is more suppressed in denser environments. This decreasing relationship becomes weaker at lower redshifts, and eventually it is reversed at present time ($z = 0$), i.e. the environmental bias increases with density on scales $2 \lesssim k \lesssim 10 h\text{Mpc}^{-1}$. This

evolutionary feature suggests that the suppression of the gas clustering becomes smaller and smaller in high-density environments compared to that in low-density environments, likely as a consequence of decreased feedback strength occurred in high-density environments at later epochs. At scales $k \gtrsim 10 h\text{Mpc}^{-1}$, processes of gas cooling and star formation come into play, and the strong dependence of the bias on the density at this scale range suggests that the strength of these processes varies in different environments.

Secondly, in Figs 8 and 9, we show the cross-correlation between the dark matter and gas distributions at different scales and in different density environments, measured by the env-WCC. This is helpful to predict the spatial distribution of dark matter from that of baryons. We find that the env-WCC in all environments converge to one at $k \lesssim 2 h\text{Mpc}^{-1}$, suggesting that distributions of the dark matter and baryonic gas are highly correlated on large scales. As the scale becomes smaller, the env-WCC becomes smaller than one, and

is also increasingly dependent on the density environment. For all redshifts we consider, on small scales, the variation of the env-WCC with density is small in low-density environments. Interestingly, in high-density environments, the env-WCC increases with density at redshift of $z = 0$, which is the exact opposite of the case at $z = 3$. This may indicate that the strength of baryonic processes in denser environments becomes smaller toward lower redshift, therefore leading to an increasing coherence between the dark matter and gas in denser environments.

Clearly, the environment-dependent statistics provide us more information than the traditional two-point statistics, and hence improving our understanding of the matter clustering. Our findings are qualitatively in agreement with those of other researches, which encourage us to further apply our method to three-dimensional fields in future works. Besides, we will also explore other applications of the continuous wavelet transform in cosmology, such as constraining cos-

mological parameters, investigating the turbulence of the intergalactic medium and analyzing the fractal properties of the large-scale structure of the universe.

ACKNOWLEDGMENTS

PH acknowledges the support by the National Science Foundation of China (No. 11947415, 12047569), and by the Natural Science Foundation of Jilin Province, China (No. 20180101228JC). In this work, we used the data from IllustrisTNG simulations. The IllustrisTNG simulations were undertaken with compute time awarded by the Gauss Centre for Supercomputing (GCS) under GCS Large-Scale Projects GCS-ILLU and GCS-DWAR on the GCS share of the supercomputer Hazel Hen at the High Performance Computing Center Stuttgart (HLRS), as well as on the machines of the Max Planck Computing and Data Facility (MPCDF) in Garching, Germany.

REFERENCES

- Addison, P. S. 2017, *The illustrated wavelet transform handbook: introductory theory and applications in science, engineering, medicine and finance*, 2nd edn. (CRC press), doi: [10.1201/9781315372556](https://doi.org/10.1201/9781315372556)
- Arizumi, N., & Aksenova, T. 2019, in *2019 IEEE International Symposium on Signal Processing and Information Technology (ISSPIT)*, 1–6
- Bacon, D. J., Battye, R. A., Bull, P., et al. 2020, *PASA*, 37, e007, doi: [10.1017/pasa.2019.51](https://doi.org/10.1017/pasa.2019.51)
- Bandura, K., Addison, G. E., Amiri, M., et al. 2014, in *Ground-based and Airborne Telescopes V*, Vol. 9145, International Society for Optics and Photonics, 914522
- Berkner, K., & Wells, R. 1997, in *Conference Record of the Thirty-First Asilomar Conference on Signals, Systems and Computers (Cat. No.97CB36136)*, Vol. 2, 1235–1239 vol.2
- Bregman, J. N. 2007, *ARA&A*, 45, 221, doi: [10.1146/annurev.astro.45.051806.110619](https://doi.org/10.1146/annurev.astro.45.051806.110619)
- Cooper, M. C., Newman, J. A., Weiner, B. J., et al. 2008, *MNRAS*, 383, 1058, doi: [10.1111/j.1365-2966.2007.12613.x](https://doi.org/10.1111/j.1365-2966.2007.12613.x)
- Cui, W., Knebe, A., Yepes, G., et al. 2018, *MNRAS*, 473, 68, doi: [10.1093/mnras/stx2323](https://doi.org/10.1093/mnras/stx2323)
- Cui, W., & Zhang, Y. 2017, in *Trends in Modern Cosmology*, ed. A. J. C. de Souza (Rijeka: IntechOpen), <https://doi.org/10.5772/68116>
- Frick, P., Beck, R., Berkhuijsen, E., & Patrickeyev, I. 2001, *MNRAS*, 327, 1145, doi: [10.1046/j.1365-8711.2001.04812.x](https://doi.org/10.1046/j.1365-8711.2001.04812.x)
- Hoyle, F., Vogeley, M. S., & Pan, D. 2012, *MNRAS*, 426, 3041, doi: [10.1111/j.1365-2966.2012.21943.x](https://doi.org/10.1111/j.1365-2966.2012.21943.x)
- Hwang, H. S., Shin, J., & Song, H. 2019, *MNRAS*, 489, 339, doi: [10.1093/mnras/stz2136](https://doi.org/10.1093/mnras/stz2136)
- Marinacci, F., Vogelsberger, M., Pakmor, R., et al. 2018, *MNRAS*, 480, 5113, doi: [10.1093/mnras/sty2206](https://doi.org/10.1093/mnras/sty2206)
- Maulbetsch, C., Avila-Reese, V., Colin, P., et al. 2007, *ApJ*, 654, 53, doi: [10.1086/509706](https://doi.org/10.1086/509706)
- Miraghaei, H. 2020, *ApJ*, 160, 227, doi: [10.3847/1538-3881/abafb1](https://doi.org/10.3847/1538-3881/abafb1)
- Mo, H., van den Bosch, F., & White, S. 2010, *Galaxy Formation and Evolution* (Cambridge University Press), doi: [10.1017/CBO9780511807244](https://doi.org/10.1017/CBO9780511807244)
- Moorman, C. M., Moreno, J., White, A., et al. 2016, *ApJ*, 831, 118, doi: [10.3847/0004-637x/831/2/118](https://doi.org/10.3847/0004-637x/831/2/118)
- Muñoz, A., Ertlé, R., & Unser, M. 2002, *Signal Process.*, 82, 749, doi: [10.1016/S0165-1684\(02\)00140-8](https://doi.org/10.1016/S0165-1684(02)00140-8)
- Naiman, J. P., Pillepich, A., Springel, V., et al. 2018, *MNRAS*, 477, 1206, doi: [10.1093/mnras/sty618](https://doi.org/10.1093/mnras/sty618)
- Nelson, D., Pillepich, A., Genel, S., et al. 2015, *Astron. Comput.*, 13, 12, doi: [10.1016/j.ascom.2015.09.003](https://doi.org/10.1016/j.ascom.2015.09.003)
- Nelson, D., Pillepich, A., Springel, V., et al. 2018, *MNRAS*, 475, 624, doi: [10.1093/mnras/stx3040](https://doi.org/10.1093/mnras/stx3040)
- Nelson, D., Springel, V., Pillepich, A., et al. 2019, *CompAC*, 6, 1, doi: [10.1186/s40668-019-0028-x](https://doi.org/10.1186/s40668-019-0028-x)
- Newburgh, L., Bandura, K., Bucher, M., et al. 2016, in *Ground-based and Airborne Telescopes VI*, Vol. 9906, International Society for Optics and Photonics, 99065X
- Omachi, M., & Omachi, S. 2007, in *2007 International Conference on Wavelet Analysis and Pattern Recognition*, Vol. 4, 1688–1691
- Patil, S., & Abel, E. W. 2009, *J Med Eng Technol*, 33, 223, doi: [10.1080/03091900802697867](https://doi.org/10.1080/03091900802697867)
- Pillepich, A., Nelson, D., Hernquist, L., et al. 2018a, *MNRAS*, 475, 648, doi: [10.1093/mnras/stx3112](https://doi.org/10.1093/mnras/stx3112)

- Pillepich, A., Springel, V., Nelson, D., et al. 2018b, MNRAS, 473, 4077, doi: [10.1093/mnras/stx2656](https://doi.org/10.1093/mnras/stx2656)
- Planck Collaboration XIII. 2016, A&A, 594, A11, doi: [10.1051/0004-6361/201526926](https://doi.org/10.1051/0004-6361/201526926)
- Rioul, O. 1991, in 1991 International Conference on Acoustics, Speech, and Signal Processing, 2213–2216 vol.3
- Springel, V. 2010, MNRAS, 401, 791, doi: [10.1111/j.1365-2966.2009.15715.x](https://doi.org/10.1111/j.1365-2966.2009.15715.x)
- Springel, V., Pakmor, R., Pillepich, A., et al. 2018, MNRAS, 475, 676, doi: [10.1093/mnras/stx3304](https://doi.org/10.1093/mnras/stx3304)
- Torrence, C., & Compo, G. P. 1998, Bull. Amer. Meteor., 79, 61, doi: [10.1175/1520-0477\(1998\)079<0061:APGTWA>2.0.CO;2](https://doi.org/10.1175/1520-0477(1998)079<0061:APGTWA>2.0.CO;2)
- Unser, M., Aldroubi, A., & Schiff, S. 1994, IEEE Trans. Signal Process, 42, 3519, doi: [10.1109/78.340787](https://doi.org/10.1109/78.340787)
- van Daalen, M. P., McCarthy, I. G., & Schaye, J. 2019, MNRAS, 491, 2424, doi: [10.1093/mnras/stz3199](https://doi.org/10.1093/mnras/stz3199)
- Vogelsberger, M., Genel, S., Springel, V., et al. 2014, Nature, 509, 177, doi: [10.1038/nature13316](https://doi.org/10.1038/nature13316)
- Vrhel, M., Lee, C., & Unser, M. 1997, IEEE Trans. Signal Process, 45, 891, doi: [10.1109/78.564177](https://doi.org/10.1109/78.564177)
- Wang, Y., & He, P. 2021, Commun. Theor. Phys., 73, 095402, doi: [10.1088/1572-9494/ac10be](https://doi.org/10.1088/1572-9494/ac10be)
- Wang, Y., Yang, H.-Y., & He, P. 2021, Analysis of matter clustering in one dimension with the Gaussian-derived wavelet. <https://arxiv.org/abs/2112.06114>
- Wang, Y., Pearce, F., Knebe, A., et al. 2018, ApJ, 868, 130, doi: [10.3847/1538-4357/aae52e](https://doi.org/10.3847/1538-4357/aae52e)
- Weinberger, R., Springel, V., Pakmor, R., et al. 2018, MNRAS, 479, 4056, doi: [10.1093/mnras/sty1733](https://doi.org/10.1093/mnras/sty1733)
- Yang, H.-Y., He, P., Zhu, W., & Feng, L.-L. 2020, MNRAS, 498, 4411, doi: [10.1093/mnras/staa2666](https://doi.org/10.1093/mnras/staa2666)
- Yang, H.-Y., Wang, Y., He, P., Zhu, W., & Feng, L.-L. 2021, MNRAS, 509, 1036, doi: [10.1093/mnras/stab3062](https://doi.org/10.1093/mnras/stab3062)